PET Functional Upcycling through Surface-Assisted Growth of Ni-BDC MOFs and Laser-Induced Carbonization towards Bend Resistive Sensor

Dmitry Kogolev[‡a], Ekaterina Kurtsevich[‡a], Maxim Fatkullin[a], Alexey Zinovyev[a], Alina Gorbunova[a], Raul D. Rodriguez[a], Olga Guselnikova[a,b], Rabah Boukherroub[c], Pavel S. Postnikov[*a,d]

‡ Equal contributors

a Research School of Chemistry and Applied Biomedical Sciences, Tomsk Polytechnic University,Tomsk 6340034, Russian Federation, postnikov@tpu.ru

b JST-ERATO Yamauchi Materials Space-Tectonics Project and International Center for Materials Nanoarchitectonics (WPI-MANA), National Institute for Materials Science (NIMS), Tsukuba, Ibaraki 305-0044, Japan

c Univ. Lille, CNRS, Univ. Polytechnique Hauts-de-France, IEMN, UMR CNRS 8520, F-59000 Lille, France

d Department of Solid-State Engineering, University of Chemistry and Technology, 16628 Prague, Czech Republic

Abstract

The growing accumulation of waste polyethylene terephthalate (PET) presents a significant environmental challenge requiring the development of sustainable recycling methods. In this study, we propose a novel approach for upcycling PET waste into bend resistive sensors through laser-assisted carbonization of surface-grown Ni-BDC (BDC = 1,4-benzenedicarboxylate). The fabrication process involves the solvothermal formation of a homogeneous Ni-BDC layer, followed by treatment with a 405 nm laser system to create a graphene-like layer with enhanced conductivity (sheet resistance 6.2 ± 3.4 Ω per square). The developed sensor demonstrates remarkable robustness, a linear response in a wide bending angle range (6 to 44º), as well as excellent mechanical stability and stiffness. This contribution paves the way for the development of cost-effective and eco-friendly devices based on low-cost polymer waste as a resource for applications in the Internet of Things.

Keywords

Functional upcycling, Polyethylene terephthalate waste, Metal-organic framework, Laser-induced graphene, Bend resistive sensor, Laser-induced carbonization, Internet of Things.

1. Introduction

In response to the pressing challenges of climate change and the ever-increasing accumulation of polymer waste [1], the concept of functional upcycling has gained significant interest in environmental engineering. Unlike conventional chemical recycling or upcycling approaches, functional upcycling aims at transforming the surface of polymer waste, offering a cost-efficient avenue for designing innovative materials, especially for energy-related applications [2–9]. The extensive utilization of readily available, low-cost polymer waste as a feedstock is promising for advancing technologies such as sensors, triboelectric generators, or supercapacitors, which are crucial for the 'Internet of Things' (IoT) [10–14]. Expanding and diversifying the range of materials obtained through functional upcycling of polymer waste is a vital task for sustainability and the circular economy.

In the functional re-/upcycling of polymer waste, polyethylene terephthalate (PET) holds a unique position, mainly due to its inherent capacity for easy conversion of the polymer backbone into reactive groups [1]. PET has exceptional properties including mechanical and chemical stability, toughness, optical transparency, processability, and

wide availability [15–20]. Despite these advantages, the ubiquity of PET leads to a dramatic increase in waste generation, with only a 30 % recycling rate [21]. At the same time, PET stands out as the most promising polymer for upcycling, whether through chemical or functional means. This is primarily due to the intrinsic reactivity of the ester groups within the polymer backbone [22–24]. Nowadays, waste PET has been used for the preparation of sorbents [25–28], membranes [29,30], and antibacterial materials [31,32]. However, its use in electronic or energy storage devices is limited due to several challenges associated with poor conductivity and thermal stability [33,34].

In addition to its use as a standalone material, PET can be transformed into terephthalic acid, a main component of the extensive family of terephthalate-based metal-organic frameworks (MOFs) [35]. This transformation has become the basis for various developments including strategies for the preparation of MOFs powder [36–42] and composite materials based on PET coated by MOFs (PET@MOF) [27,33,43–46], designed for sustainable applications. As a promising upcycling pathway, PET, PET@MOF, and PET-derived MOFs are pyrolyzed to create carbon-based materials for sensors and energy-related applications [38,47,48–55,56]. However, these approaches typically require significant energy consumption, an inert atmosphere, and post-processing to obtain the final device [38,50]. Enhancing the carbonization process has been achieved by the application of lasers to directly produce graphene-like materials from thin films of MOFs immobilized on suitable substrates [57–60]. In these cases, the device's performance is predetermined by the laser irradiation regime and specific patterns obtained by laser-scribing [58,59]. Despite the technological feasibility, devices produced by laser-assisted carbonization of MOFs suffer from poor mechanical properties because of the low adhesion of the carbonized material to the substrate [58]. These limitations compromise the widespread use of upcycled waste PET materials in construction and energy applications, where mechanical robustness plays a key role. Thus, the transition in energy-related device manufacturing should focus on innovative processes that enable the deliberate design of mechanically durable devices at minimal operational costs, making effective use of readily available waste feedstock.

Recently, we introduced a functional upcycling strategy for waste PET, involving laser-assisted processing of surface-grown terephthalate MOFs [46]. Here we build upon this strategy expanding to energy-related devices to create bending sensors directly from waste PET by a laser scribing procedure (Fig. 1). This novel sensor has impressive mechanical stability and stiffness, making it suitable for applications in construction and

building. Moreover, the technological feasibility of this process opens the door to the broader development of waste PET-derived sensors.

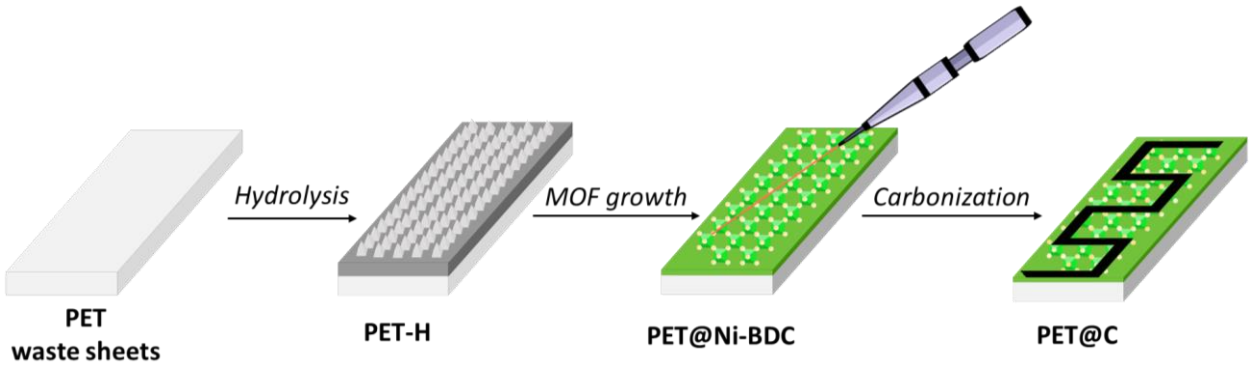

Fig. 1. Strategy for PET@C preparation from PET waste *via* PET hydrolysis, Ni-BDC PET surface growth, and laser scribing process by 405 nm irradiation.

2. Results and discussion

2.1 Preparation of PET@Ni-BDC

Our investigation began with the development of a rational approach towards creating a hybrid material with surface-grown Ni-BDC (where BDC = 1,4-benzenedicarboxylate) MOFs, primarily due to the cost advantages of this method compared to UiO-66 (Fig. 2A). To achieve this, we adopted a recently reported method that involved the hydrolysis of waste PET surfaces by acid treatment followed by the solvothermal growth of MOFs [46]. In the first step, waste PET sheets were washed and cut into 1.0 × 3.0 cm^2 pieces. These prepared wafers underwent surface hydrolysis by concentrated sulfuric acid to introduce –COOH groups onto the PET surface, which are essential for subsequent surface-assisted nucleation with nickel ions (Section 2, ESI†). The formation of –COOH groups was confirmed by Fourier-transform infrared (FTIR) spectroscopy and X-ray photoelectron spectroscopy (XPS), with additional details provided in Section 2, ESI†.

The activation of the waste PET surface during hydrolysis allowed for the direct growth of Ni-BDC MOF on the wafers. We adopted a previously published method in which Ni-BDC was synthesized under solvothermal conditions by mixing a nickel precursor with terephthalic acid derived from waste PET bottles [40] in *N*,*N*-dimethylformamide (DMF) (details are provided in Section 3, ESI†) [61]. We initially tried the conventional method that involves 15 hours of heating, as reported earlier (Section 3, ESI†) [61]. Unfortunately, this led to the formation of thick, detached, and inhomogeneous Ni-BDC layers, which could negatively affect the subsequent laser-induced carbonization

(Fig. S4A and B, ESI†). To overcome this issue, we decreased the precursor loading by half, but unfortunately, the same issues persisted (Fig. S4C and D, ESI†). Finally, we succeeded in the preparation of the desired PET@Ni-BDC material by optimizing the reaction time. The formation of a uniform thin layer of Ni-BDC on the hydrolyzed PET surface was observed after just 5 hours of heating (Fig. S4E and F, ESI†). The final optimized procedure includes the growth of Ni-BDC directly on hydrolyzed PET sheets under solvothermal conditions. It is worth noting that we used a reduced amount of reagents and processing time, making the process more economically and energetically efficient.

2.2 Characterization of PET@Ni-BDC

The formation of the Ni-BDC layer on PET sheets was confirmed by a series of spectroscopic analyses. FTIR spectra of pristine, hydrolyzed PET, and PET sheets coated by Ni-BDC, and Ni-BDC powder are presented in Fig. 2B. In the spectrum of pristine PET, we observed the characteristic peaks at 1712 and 1240 cm^{-1} associated with C=O bonds (see full peak assignment in Table S1, ESI†). After hydrolysis, we observed a new peak at 2960 cm^{-1} confirming the presence of –COOH groups on the surface (Fig. 2B) [62,63]. Following the growth of Ni-BDC on PET, we observed characteristic peaks corresponding to COO–Ni groups, which exhibited symmetric (1366 cm^{-1}) and asymmetric (1582 cm^{-1}) vibrations of COO^- (Fig. 2B) [64]. The FTIR data of PET@Ni-BDC is in agreement with that of Ni-BDC powder and previously published data (Table S2, ESI†) [65].

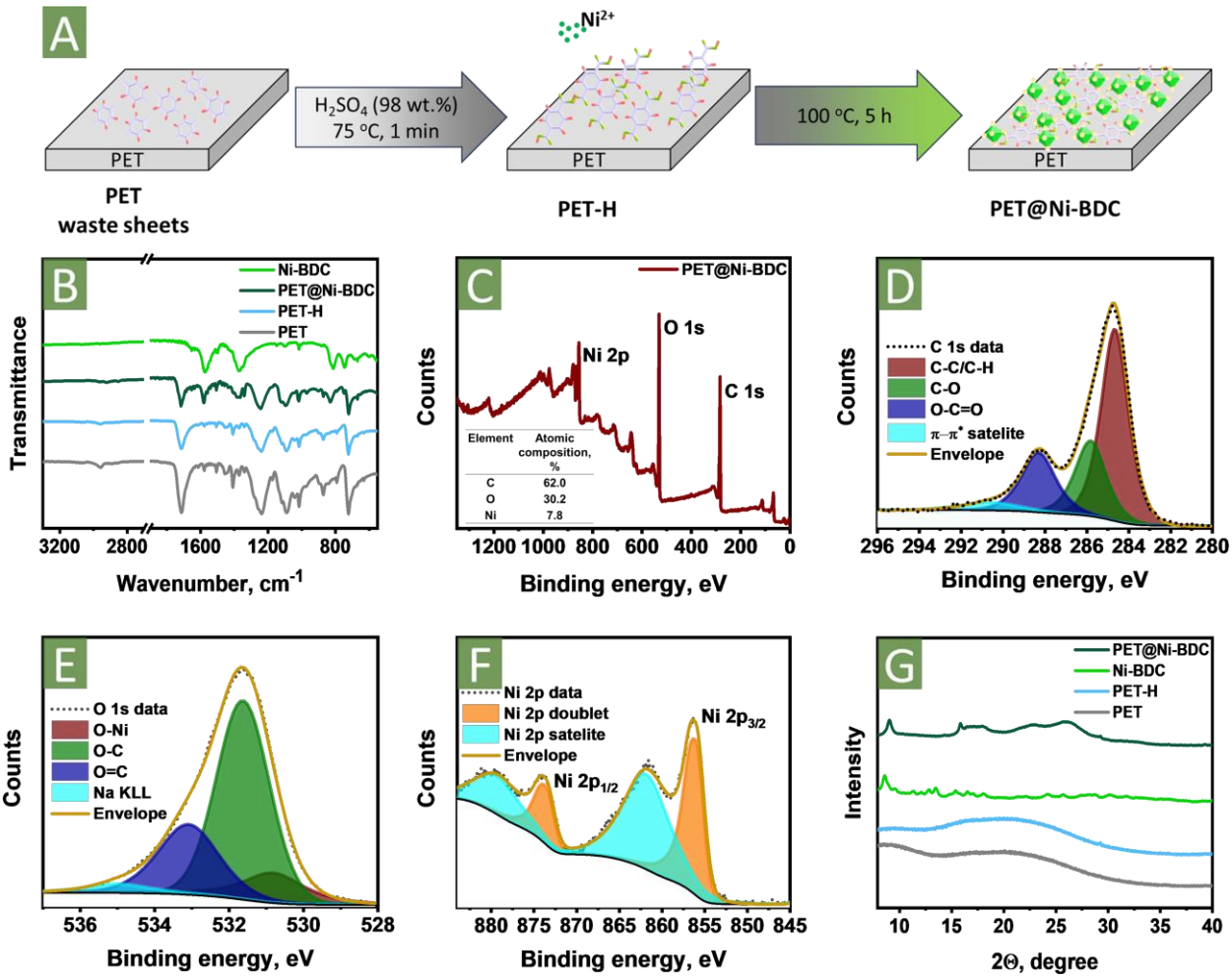

Fig. 2. (**A**) Scheme of PET@Ni-BDC preparation *via* PET hydrolysis and Ni-BDC growth. (**B**) FTIR spectra of pristine and hydrolyzed PET, PET@Ni-BDC, and Ni-BDC powder. Characterization of PET@Ni-BDC by XPS: (**C**) survey spectrum and core level spectra of (**D**) C 1s, (**E**) O 1s, and (**F**) Ni 2p. (**G**) XRD patterns of pristine (grey), hydrolyzed (blue), coated by Ni-BDC PET sheets (olive), and Ni-BDC (green).

We investigated the chemical compositions of PET@Ni-BDC and intermediate products by XPS (Fig. 2C-F). The hydrolysis of PET resulted in an increase in the C=O component intensity on the O 1s deconvoluted peak (533.0 eV, Fig. S3C and F, ESI†) due to the formation of –COOH groups. The subsequent growth of Ni-BDC led to drastic changes in the surface chemical composition. The XPS survey scan revealed the appearance of a Ni^{2+} related peak (Fig. 2C), indicating the presence of 7.8 at.% of Ni [66]. The C 1s peak deconvolution showed the same chemical state as PET and PET-H (Fig. 2D and S3B,E, ESI†). However, on the O 1s deconvoluted peak, we observed the appearance of the O–Ni component at 530.8 eV, along with a notable decrease in the O=C component intensity (533.1 eV, Fig. 2E).

In the high-resolution Ni region spectrum, we identified Ni $2p_{3/2}$ at 856.1 eV and Ni $2p_{1/2}$ at 873.6 eV peaks, along with corresponding shake-up satellites attributed to the Ni $2p_{3/2}$ at 861.8 eV and Ni $2p_{1/2}$ at 879.3 eV of Ni^{2+} (Fig. 2F) [66]. The localization of Ni-related peaks is in good agreement with the high-resolution spectra of Ni-BDC powder (Fig. S5D, ESI†).

We evaluated the crystallinity of the materials using X-ray diffraction analysis (XRD) (Fig. 2G). PET and hydrolyzed PET showed an amorphous structure without well-distinguishable reflections (Fig. 2G) [46,67]. However, after the growth of Ni-BDC, we observed discernable diffractions at 9 and 16°, corresponding to Ni-BDC [68], confirming the formation of the PET@Ni-BDC composite.

The surface morphology of prepared materials and distribution of Ni-BDC crystallites across the material's surface were investigated by scanning electron microscopy with energy-dispersive X-ray (SEM-EDX) analysis (Fig. 3A-D). Pristine PET exhibited a smooth surface without significant defects or features (Fig. 3A). Hydrolysis led to the formation of clearly visible cracks and cavities across the whole surface (Fig. 3B). Surface-assisted growth of Ni-BDC resulted in drastic changes in surface morphology, with cracks and features uniformly covered by Ni-BDC crystallites (Fig. 3C). The MOF layer was composed of aggregated polyhedral nanoparticles with an average size of ~2.5 – 3.0 µm, consistent with the shape of Ni-BDC crystals prepared by the same method (Fig. S6A and B, ESI†). EDX mapping results confirmed the homogeneous nickel distribution with a relatively high Ni concentration (approx. 23.6 %) (Fig. 3D).

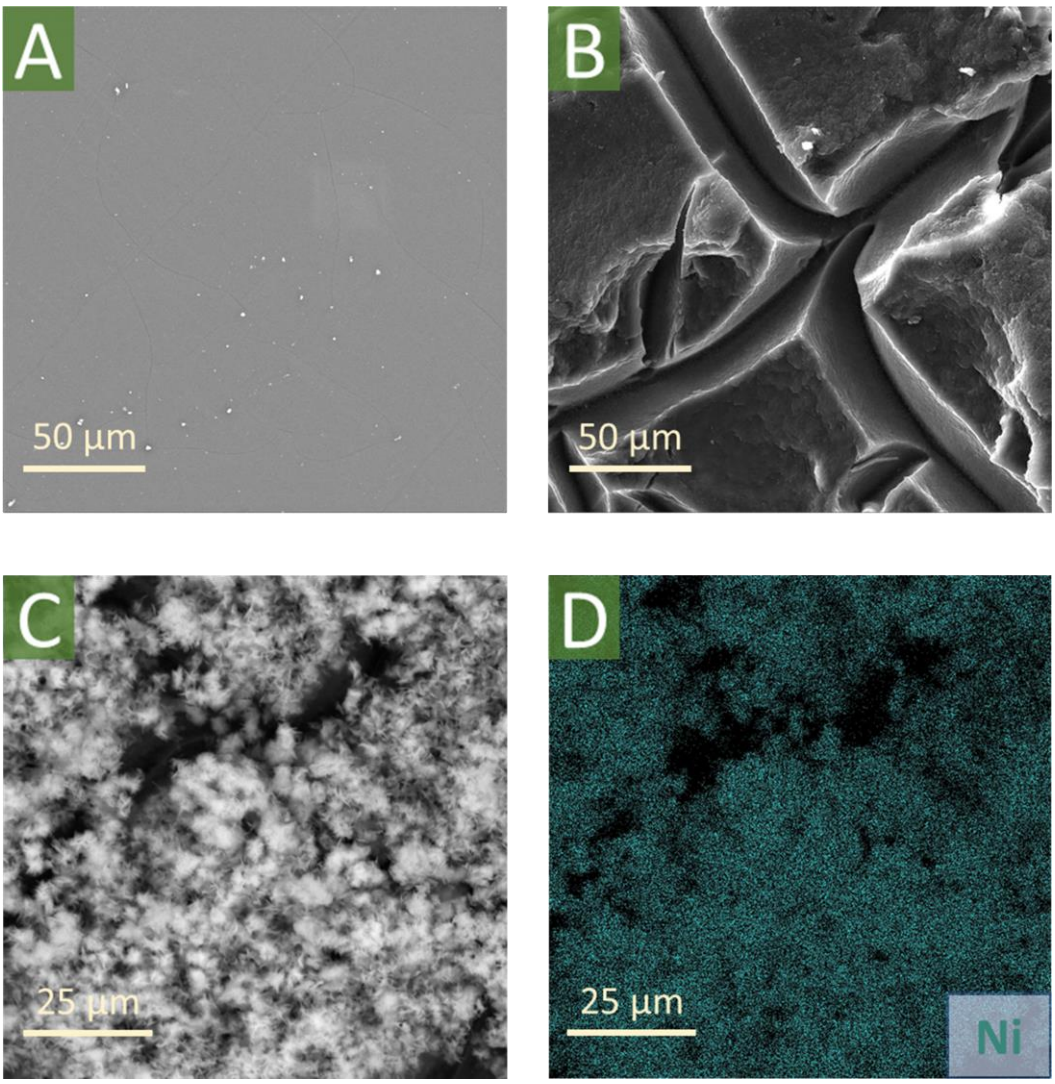

Fig. 3. SEM images of (**A**) pristine PET sheets, (**B**) hydrolyzed PET sheets, (**C**) PET@Ni-BDC. (**D**) SEM-EDX map of Ni across PET@Ni-BDC.

2.3 Laser-induced carbonization of PET@Ni-BDC

The next crucial step of our strategy for functional upcycling of PET waste was the laser treatment of the PET@Ni-BDC surface to generate of PET@C composite (Fig. 4A and B). We recorded the absorbance spectrum of PET@Ni-BDC to determine the optimal laser wavelength for our process (Fig. 4C). Notably, the main absorbance maximum at 395 nm was not observed for pristine or hydrolyzed PET (Fig. S2, ESI†). This absence indicated the potential for selective carbonization of the MOF layer without significant interaction between the laser beam and non-functionalized PET. Based on the absorbance spectra, we selected a 405 nm LED source (pulse frequency = 1.6 kHz, power = 1500 mW) integrated into a commercially available NEJE DK-8-KZ laser engraving system. This choice offered several advantages over traditional femtosecond

lasers, including availability, cost-effectiveness, and the capability to process a larger area of material [69].

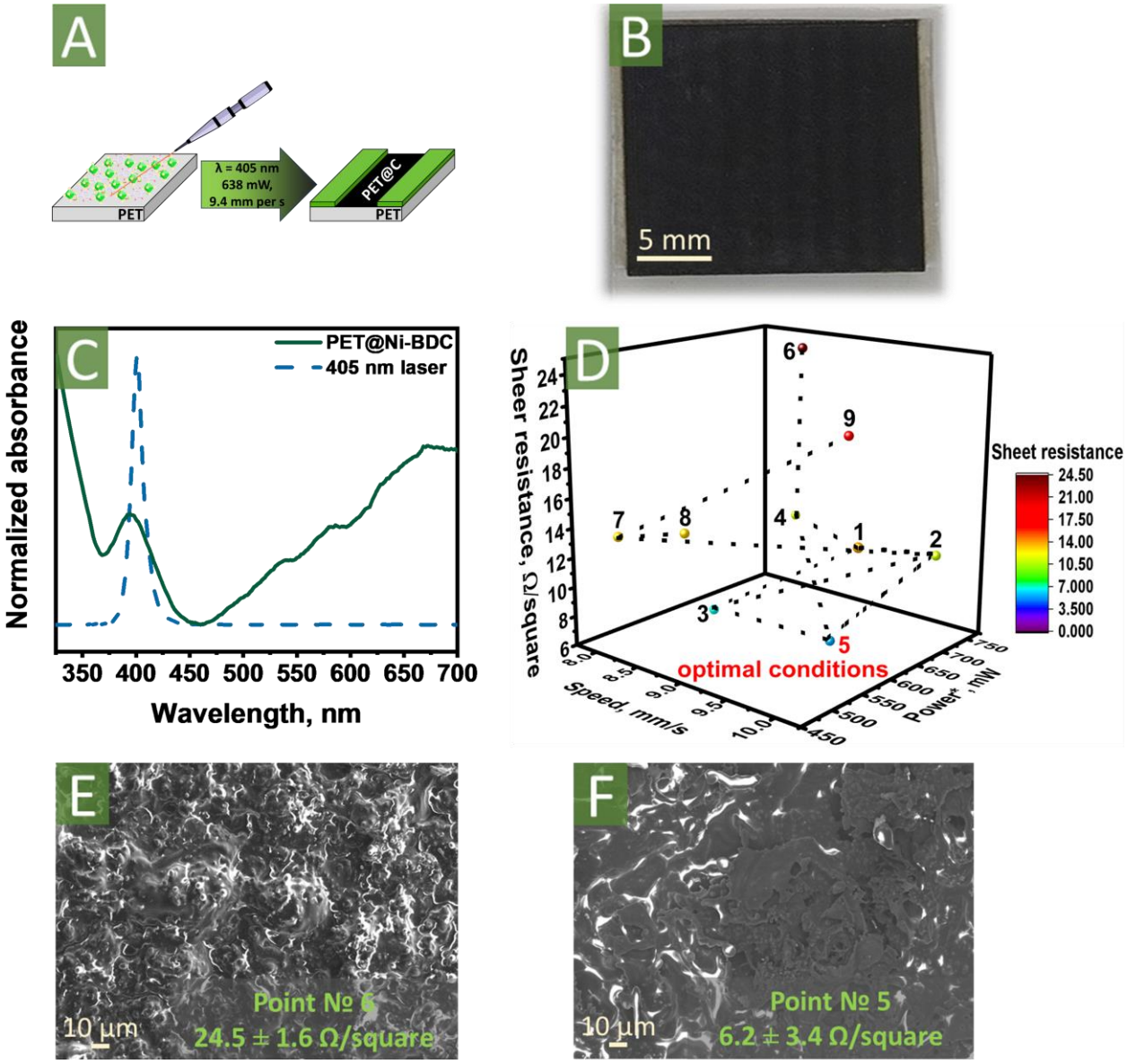

Fig. 4. (**A**) Scheme of PET@Ni-BDC laser treatment. (**B**) PET@C image. (**C**) UV-vis spectra of PET@Ni-BDC (the dashed line represents the excitation wavelength of 405 nm laser). (**D**) Optimization of PET@Ni-BDC laser treatment by Nelder-Mead method. *Nominal laser power. SEM image of PET@C after laser treatment under starting (**E**) and optimal (**F**) conditions.

In our first laser processing experiment on PET@Ni-BDC, we used a laser beam with a movement speed of 9.9 mm per s and an irradiation power of 600 mW [46]. The laser path is schematically illustrated in Fig. S7, ESI†. We observed the selective carbonization of PET@Ni-BDC at the point of contact between the laser beam and the

material's surface. After the laser treatment, we obtained a uniform black layer on the PET surface characterized by a low sheet resistance of 14.0 ± 2.9 Ω per square, indicating its potential applicability as a bending sensor.

To further optimize the laser processing conditions, we employed the Nelder-Mead method, varying the laser power and laser movement speed (Fig. 4D, Table S3; see Section 4, ESI† for details). Surface resistance serves as a crucial indicator of carbonization efficiency, reflecting the uniformity of the carbon layer and the potential applicability of the resulting material. We started the optimization process by selecting three random points in a triangular parametric shape to adjust two laser parameters (points 1-3, Fig. 4D). The highest conductivity values were measured at the vertices of the triangle, operations like reflection, compression, and stretching of the triangle. The top with the lowest conductivity was significantly reduced in electrical resistance. Consequently, we observed the formation of a rough surface in a material with a relatively high sheet resistance of 24.5 ± 1.6 Ω per square (Fig. 4E). Through this optimization process, we achieved a considerable reduction in sheet resistance to 6.2 ± 3.4 Ω per square (Fig. 4F). Thus, the optimal conditions were determined as a laser beam scanning at a speed of 9.4 mm per s with a laser power of 638 mW. It is worth noting that the PET@C material, obtained through this optimization, exhibited one of the highest electrical conductivities among similar graphene-based coatings prepared by laser treatment (Table 1).

Table 1. Sheet resistance comparison of untreated and reduced GO and graphene materials produced by laser-induced carbonization

Materials and methods	Laser information	Applied power	Sheet resistance, Ω per square	References
Pristine GO	–	–	10^6–10^{10}	[70–72]
Deposition of GO on a cotton fabric followed by reduction by hot press	–	–	900	[73]

Laser-induced graphene on polyimide	CO_2 laser	13 mW per cm^2	733–1100	[74]
Laser-induced graphene on polyimide	UV laser, 355 nm, pulse frequency 150 kHz, scanning speed of 50 mm per s	3 W	$1.5 \cdot 10^2$–$3 \cdot 10^5$	[75]
Laser-induced graphene on polyimide	UV pulsed laser, 355 nm, pulse frequency 30 kHz	–	0.44	[76]
Laser-induced graphene on polyimide	CO_2 laser, 365 nm, scanning speed of 1 mm per s	4.7–7.0 mW	15	[77]
Laser-reduced graphene oxide in liquid nitrogen environment	Picosecond pulsed laser: 1064 nm, pulse duration 10 ps, 100 kHz repetition rate, spot size 30 μm	–	50–60	[78]
Laser direct patterning of reduced GO on flexible (PET) substrate by femtosecond pulses	Femtosecond 515 nm laser, 280 fs pulse length, 500 kHz repetition rate	35–45 nJ pulse energy with 10–20 pulses per μm	200.0	[79]
Polyimide surface carbonization	CO_2 laser	4.5 to 8.25 W	60.0	[80]

Polyimide surface carbonization	CO_2 with 10.6 μm wavelength and a beam size of 0.127 mm	25 W	30 ± 2.6	[81]
Poly (Ph-ddm)-surface carbonization	CO_2 laser 10.6 μm, pulse frequency is 20 kHz	20 W	35.0	[82]
Laser-induced graphitization of ink based on cellulose and lignin	CO_2 laser 10.6 μm	3.3 W	3.8 ± 0.1	[83]
Carbonization of MOFs powder (LIC-(ZIF-8) and LIC-(ZIF-67))	CO_2 laser 1064 nm	4.8 W	Approximately 125	[58]
Low-cost laser carbonization (LIMPc)	450 nm LED pulse laser	580 mW	181	[84]
Low-cost laser carbonization (PET@LB-UiO-66)	405 nm LED pulse laser	735 mW	10.4 ± 3.1	[46]
Low-cost laser carbonization (PET@C)	405 nm LED pulse laser	638 mW	6.2 ± 3.4	This work

2.4 Characterization of PET@C

The PET@C material, prepared under optimized conditions, was characterized by Raman spectroscopy. After the laser treatment of PET@Ni-BDC, we observed the disappearance of spectral features associated with the Ni-BDC structure (1133, 1172, 1424, 1555, and 1724 cm^{-1}) (Fig. 5A). Instead, the Raman spectrum of PET@C revealed

distinctive peaks at 1350 and 1583 cm^{-1}, attributed to the D and G peaks of graphene-like materials [85]. The presence of few-layered graphene sheets impregnating the polymer matrix was evidenced by the characteristic 2D mode fingerprint at 2699 cm^{-1}. Furthermore, the relatively high-intensity ratio (I_D/I_G = 0.96) indicated a high graphitization degree, explaining the material's low sheet resistance.

The full conversion of the Ni@BDC layer was confirmed by FTIR. After treatment, we observed the disappearance of Ni-BDC-related vibration bands (symmetric and asymmetric stretch vibrations of COO–Ni bonds at 1366 and 1582 cm^{-1}, respectively) (Fig. S8 and Table S4, ESI†). However, the characteristic bands of PET remained visible, confirming the formation of the composite material, with PET as a matrix and carbonized Ni-BDC as the filler.

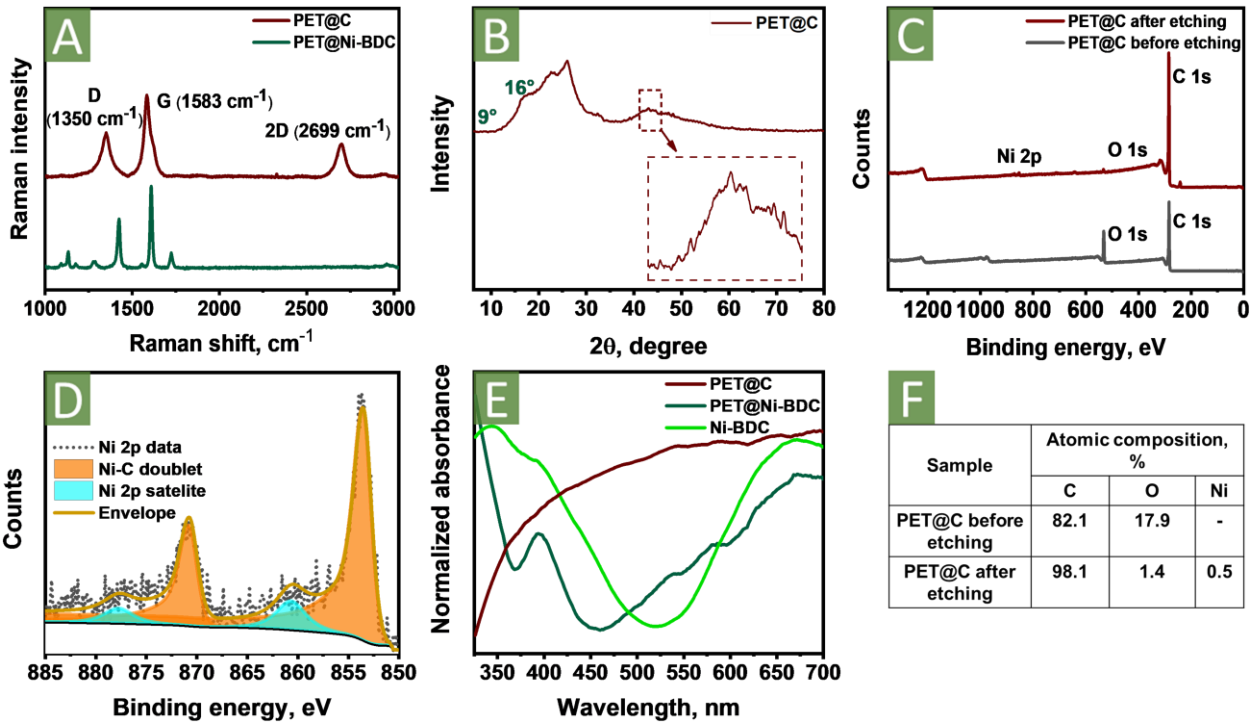

Sample	Atomic composition, %		
	C	O	Ni
PET@C before etching	82.1	17.9	-
PET@C after etching	98.1	1.4	0.5

Fig. 5. Characterization of PET@C: (**A**) Raman spectra, (**B**) XRD patterns, XPS: (**C**) survey spectra before and after Ar^+ surface etching, and (**D**) core level spectrum of the Ni 2p region after Ar^+ surface etching, (**E**) UV-vis spectra, (**F**) atomic composition table from (C).

The full conversion of Ni-BDC crystals was further evidenced by XRD, demonstrating the disappearance of Ni-BDC characteristic peaks at 9 and 16° (Fig. 5B) [68]. At the same time, we observed the peak at 43°, suggesting the formation of Ni_3C (Fig. 5B, insert) [86]. Generally, the formation of metal carbides during the carbonization

of MOFs was observed recently by our group [46] and Deng's group [87] and also in laser processing of Al nanoparticles on PET [88].

The chemical composition of PET@C was analyzed by XPS (Fig. 5C,F and S9A-C, ESI†). The survey scan revealed changes in surface element concentrations, with an increase in carbon (from 62.0 to 82.1 at.%), a decrease in oxygen (from 30.2 to 17.9 at.%), and the disappearance of nickel (Fig. 5C and F). The C 1s peak deconvolution confirmed the presence of the sp^2 hybridization component (283.3 eV) in addition to the C–C/C–H species, differentiating PET@C from PET@Ni-BDC (Fig. S9A, ESI†). These results evidenced the formation of laser-induced graphene along with fused PET upon laser treatment, in agreement with Raman spectroscopy results. The O 1s core level spectrum revealed the disappearance of the O–Ni component, a decrease in the O–C component, and an increase in the O=C component intensity (Fig. S9B, ESI†). Surprisingly, no Ni-related peaks were observed during the initial analysis of PET@C due to the limited XPS penetration depth of just a few nanometers and the Ni distribution after laser scribing (Fig. S9C, ESI†).

To overcome this depth limitation, we employed a monatomic Ar^+ depth-profiling technique to etch the surface, followed by XPS analysis (Fig. 5C,D,F and S9D,E, ESI†). The survey scan revealed a sufficient increase in carbon (from 82.1 to 98.1 at.%) and a decrease in oxygen concentrations (from 17.9 to 1.4 at.%), along with the appearance of nickel (0.5 at.%) (Fig. 5C and F). The C 1s peak deconvolution showed the disappearance of the C–C/C–H components, and a significant decrease in the C=O band (Fig. S9D, ESI†). On the O 1s deconvoluted peak, we observed a considerable decrease in all component intensities (Fig. S9E, ESI†). The presence of Ni $2p_{3/2}$ at 853.5 eV and Ni $2p_{1/2}$ at 870.8 eV peaks indicated the formation of nickel carbide in the resulting material (Fig. 5D) [89].

Furthermore, we obtained UV-vis spectroscopy results that revealed increased absorbance throughout the visible region compared to Ni-BDC and PET@Ni-BDC (Fig. 5E). The band gap (E_g) underwent significant changes due to the formation of graphene-like domains (Fig. S10, ESI†), as reported previously for MOFs carbonization [90]. In our case, the value of E_g for PET@C was calculated as 0.406 eV (Fig. S10C, ESI†), which is much less compared to Ni-BDC MOF (2.980 eV, Fig. S10A, ESI†) and PET@Ni-BDC (3.037 eV, Fig. S10B, ESI†). These changes suggest the generation of a material with potential applications in solar desalination, solar photodegradation of pollutants, solar atmospheric water harvesting, *etc.* [91].

Morphological analysis of the PET@C composite through SEM-EDX (Fig. 6A and B) revealed drastic changes in PET@Ni-BDC surface morphology after laser treatment. Microcrystalline Ni-BDC structures transformed into a relatively smooth porous surface (Fig. 6A). The formation of pores resulted from the release of CO_2 during the decarboxylation of terephthalates [69]. EDX analysis of the treated surface revealed a homogenous distribution of Ni across the entire surface without significant particle agglomeration (Fig. 6B).

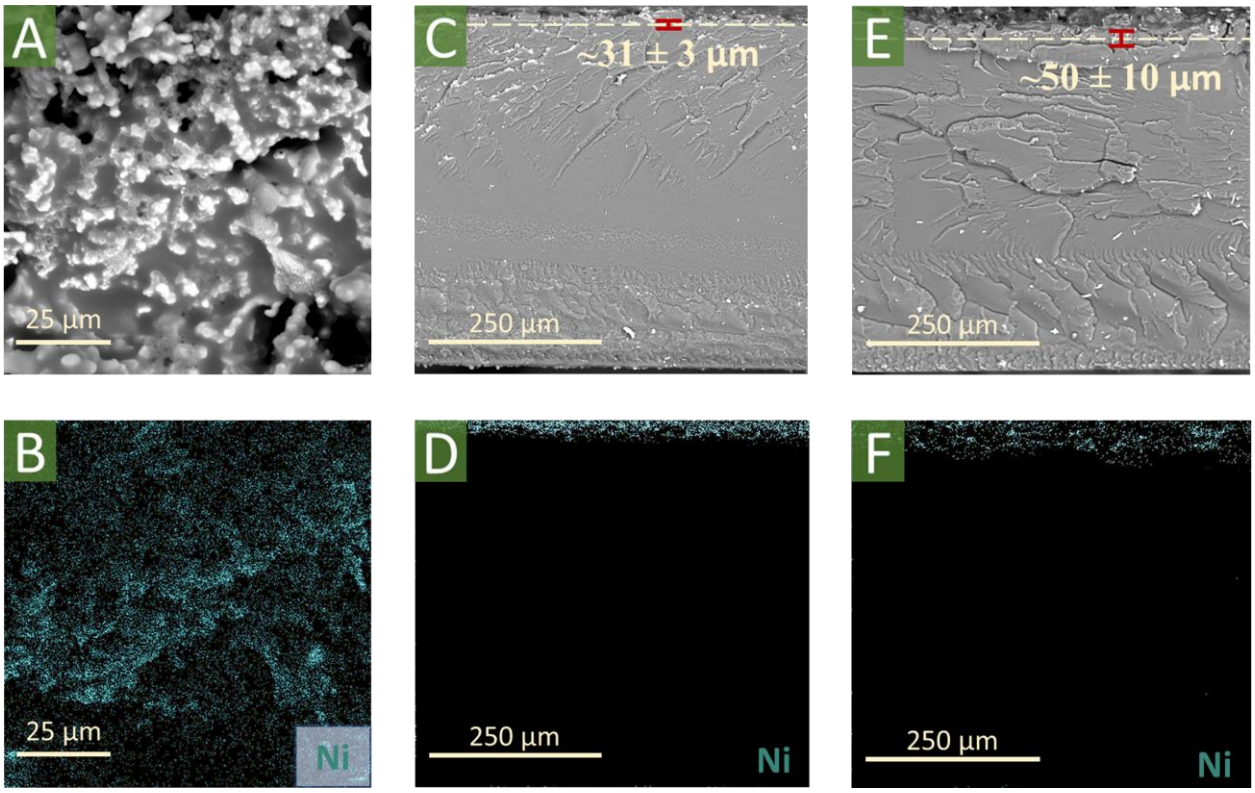

Fig. 6. Morphology investigation of PET@C: (**A**) SEM image, (**B**) EDX mapping of Ni. Cross-sectional SEM-EDX images of (**C,D**) PET@Ni-BDC and (**D,F**) PET@C.

We used SEM combined with EDX analysis to evaluate the thickness and Ni_3C distribution in the carbonized layer. The composite thickness measured approximately 50 ± 10 µm, which is larger than the thickness of the Ni-BDC layer (31 ± 3 µm). This observation aligns with a general mechanism we observed for UiO-66 [46], indicating a common process for PET@MOFs carbonization. This process involves the complex interplay of secondary melting of PET with the simultaneous formation of the composite (Fig. 6C and E). Moreover, the formation of pores throughout the composite layer was clearly observed (Fig. S11, ESI†). EDX analysis showed a concentration of Ni on the top layer for PET@Ni-BDC (Fig. 6D). In contrast, PET@C exhibited a relatively homogenous

distribution of Ni in the vertical direction, suggesting the embedding of particles during the melting of the PET matrix (Fig. 6F).

2.5 Testing of PET@C as a bending resistive sensor

The next step of our research was to study the possibility of using the PET@C material as the active component of a flexible resistive sensor (Fig. 7A and S12, ESI†). The bending sensor exhibited a clear, distinguishable, and reproducible response to bending angles. As the bending angle increased, a corresponding increase in relative resistance changes, demonstrating a linear response of 18 ± 1 % up to 44º was recorded (Fig. 7B). Moreover, we investigated the sensor performance under 1000 bending cycles, simulating long-term use for online monitoring in wearables and IoT applications (Fig. 7C). The sensor's response remained stable during the whole test, with only a ~3 % difference between the starting point and the end of the long-term durability tests, indicating the sensor's robustness and stability during cycling bending (Fig. 7C, insert). To assess the mechanical properties and durability of the PET@C composite, we conducted tensile strength tests (Fig. 7D). Ultimate tensile strength (UTS) was evaluated at a strain rate of 10 mm per min. The UTS of PET@C significantly increased from 38.2 to 57.1 MPa, with the same elongation of 5.4 % compared to pristine PET (Fig. 7D). This enhancement can be attributed to PET surface melting during laser-induced transformations of surface-grown Ni-BDC and formation of the carbon-based material composite [92].

Our findings suggest the potential use of the PET@C composite as a flexible resistive sensor, with promising applications in smart wearable devices [48,93,94], personalized health monitoring [95], electronic skin [96], human-machine interfaces [97], and more.

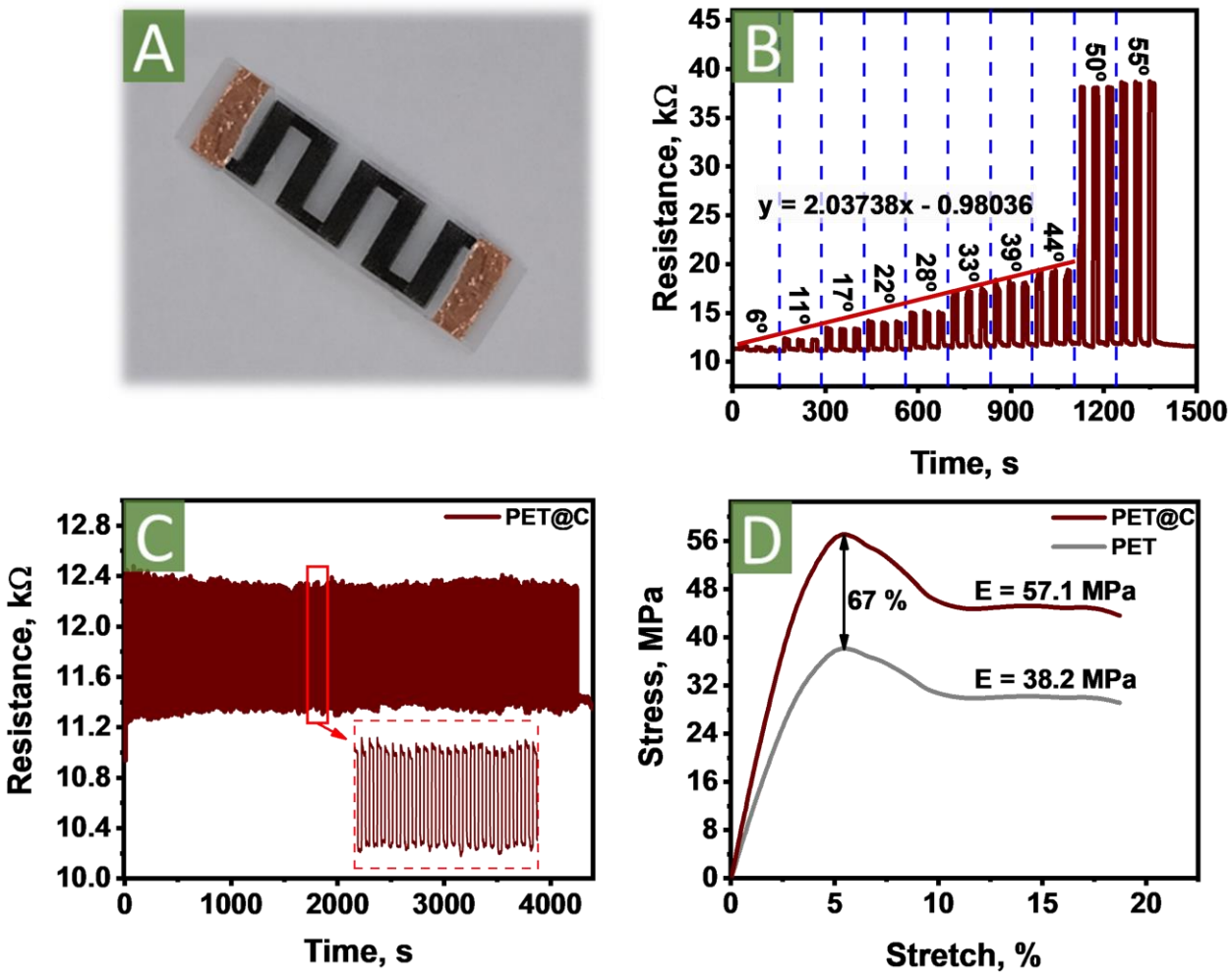

Fig. 7. (**A**) Images of the sensor. Resistive characterization of the PET@C bending sensor: (**B**) resistance response to the bending depth and (**C**) long-term durability testing for 1000 stretching and releasing cycles. (**D**) Ultimate tensile strength measurements of PET and PET@C.

3. Conclusion

In summary, we introduced a convenient and low-cost strategy for the functional upcycling of waste PET into bend resistive sensors, offering a sustainable solution to address the plastic waste problem. By repurposing PET, a readily available and inexpensive material, it was successfully transformed into a value-added bend sensor with notable features including enhanced conductivity (sheet resistance 6.2 ± 3.4 Ω per square), robustness, linear response over a wide range of bending angles (from 6 to 44º), as well as mechanical stability and stiffness. These properties were achieved through a two-step process involving the surface-assisted growth of Ni-BDC and subsequent laser-induced carbonization. The combination of these procedures resulted in PET sheets coated with a laser-induced graphene/nickel carbide layer, which exhibits excellent electrical conductivity and sensitivity to bending forces. This breakthrough offers new

possibilities for the successful development of bend resistive sensors in various fields, including wearable electronics, robotics, and healthcare. The ability to transform waste PET into functional sensors not only contributes to reducing environmental pollution but also offers cost-effective sensing solutions for the Internet of Things.

Conflicts of interests

There are no conflicts to declare.

Acknowledgements

The authors thank the central laboratories of TPU (Analytical center) for XPS measurements and Tomsk Regional Core Shared Research Facilities Center of National Research Tomsk State University and Science Park of St. Petersburg State University for SEM. The research has been financially supported by the Ministry of High Education and Science of Russian Federation № 075-15-2022-244 (Russian-French project in the frame of PHC ‘‘Kholmogorov’’).

References

[1] O. Guselnikova, O. Semyonov, E. Sviridova, R. Gulyaev, A. Gorbunova, D. Kogolev, A. Trelin, Y. Yamauchi, R. Boukherroub, P. Postnikov, “Functional upcycling” of polymer waste towards the design of new materials, Chem. Soc. Rev. 52 (2023) 4755–4832. https://doi.org/10.1039/D2CS00689H.

[2] M. Jiang, X. Wang, W. Xi, H. Zhou, P. Yang, J. Yao, X. Jiang, D. Wu, Upcycling plastic waste to carbon materials for electrochemical energy storage and conversion, Chem. Eng. J. 461 (2023) 141962. https://doi.org/10.1016/j.cej.2023.141962.

[3] C. Jehanno, J.W. Alty, M. Roosen, S. De Meester, A.P. Dove, E.Y.-X. Chen, F.A. Leibfarth, H. Sardon, Critical advances and future opportunities in upcycling commodity polymers, Nature. 603 (2022) 803–814. https://doi.org/10.1038/s41586-021-04350-0.

[4] H. Chen, K. Wan, Y. Zhang, Y. Wang, Waste to Wealth: Chemical Recycling and Chemical Upcycling of Waste Plastics for a Great Future, ChemSusChem. 14 (2021) 4123–4136. https://doi.org/10.1002/cssc.202100652.

[5] B. von Vacano, H. Mangold, G.W.M. Vandermeulen, G. Battagliarin, M. Hofmann, J. Bean, A. Künkel, Sustainable Design of Structural and Functional Polymers for a Circular Economy, Angew. Chemie Int. Ed. 62 (2023). https://doi.org/10.1002/anie.202210823.

[6] B. Wang, Y. Wang, S. Du, J. Zhu, S. Ma, Upcycling of thermosetting polymers into high-value materials, Mater. Horizons. 10 (2023) 41–51. https://doi.org/10.1039/D2MH01128J.

[7] Ł. Zedler, S. Wang, K. Formela, Ground tire rubber functionalization as a promising approach for the production of sustainable adsorbents of environmental pollutants, Sci. Total Environ. 836 (2022) 155636. https://doi.org/10.1016/j.scitotenv.2022.155636.

[8] H. Jung, G. Shin, H. Kwak, L.T. Hao, J. Jegal, H.J. Kim, H. Jeon, J. Park, D.X. Oh, Review of polymer technologies for improving the recycling and upcycling efficiency of plastic waste, Chemosphere. 320 (2023) 138089. https://doi.org/10.1016/j.chemosphere.2023.138089.

[9] Z. Chen, W. Wei, B.-J. Ni, H. Chen, Plastic wastes derived carbon materials for green energy and sustainable environmental applications, Environ. Funct. Mater. 1 (2022) 34–48. https://doi.org/10.1016/j.efmat.2022.05.005.

[10] J.A. Cardenas, J.B. Andrews, S.G. Noyce, A.D. Franklin, Carbon nanotube electronics for IoT sensors, Nano Futur. 4 (2020) 012001. https://doi.org/10.1088/2399-1984/ab5f20.

[11] W.L. Lai, S. Sharma, S. Roy, P.K. Maji, B. Sharma, S. Ramakrishna, K.L. Goh, Roadmap to sustainable plastic waste management: a focused study on recycling PET for triboelectric nanogenerator production in Singapore and India, Environ. Sci. Pollut. Res. 29 (2022) 51234–51268. https://doi.org/10.1007/s11356-022-20854-2.

[12] R. Mendoza, J. Oliva, K.P. Padmasree, A.I. Oliva, A.I. Mtz-Enriquez, A. Zakhidov, Highly efficient textile supercapacitors made with face masks waste and thermoelectric Ca3Co4O9-δ oxide, J. Energy Storage. 46 (2022) 103818. https://doi.org/10.1016/j.est.2021.103818.

[13] W. Zuo, L. Zang, Q. Liu, J. Qiu, M. Lan, C. Yang, A quasi-solid-state supercapacitor based on waste surgical masks with high flexibility and designable shape, Colloids Surfaces A Physicochem. Eng. Asp. 634 (2022) 128020. https://doi.org/10.1016/j.colsurfa.2021.128020.

[14] X. Ren, H. Fan, J. Ma, C. Wang, Y. Zhao, S. Lei, Triboelectric Nanogenerators Based on Fluorinated Wasted Rubber Powder for Self-Powering Application, ACS Sustain. Chem. Eng. 5 (2017) 1957–1964. https://doi.org/10.1021/acssuschemeng.6b02756.

[15] M.N. Ezzat, Z.T.A. Ali, Green approach for fabrication of graphene from polyethylene terephthalate (PET) bottle waste as reactive material for dyes removal from aqueous solution: Batch and continuous study, Sustain. Mater. Technol. 32 (2022) e00404. https://doi.org/10.1016/j.susmat.2022.e00404.

[16] Y. Zhang, L. Ying, Z. Wang, Y. Wang, Q. Xu, C. Li, Unexpected hydrophobic to hydrophilic transition of PET fabric treated in a deep eutectic solvent of choline chloride and oxalic acid, Polymer (Guildf). 234 (2021) 124246. https://doi.org/10.1016/j.polymer.2021.124246.

[17] R. Nisticò, Polyethylene terephthalate (PET) in the packaging industry, Polym. Test. 90 (2020) 106707. https://doi.org/10.1016/j.polymertesting.2020.106707.

[18] V. Dhaka, S. Singh, A.G. Anil, T.S. Sunil Kumar Naik, S. Garg, J. Samuel, M. Kumar, P.C. Ramamurthy, J. Singh, Occurrence, toxicity and remediation of polyethylene terephthalate plastics. A review, Environ. Chem. Lett. 20 (2022) 1777–1800. https://doi.org/10.1007/s10311-021-01384-8.

[19] A.K. Singh, R. Bedi, B.S. Kaith, Composite materials based on recycled

polyethylene terephthalate and their properties – A comprehensive review, Compos. Part B Eng. 219 (2021) 108928. https://doi.org/10.1016/j.compositesb.2021.108928.

[20] T. Sang, C.J. Wallis, G. Hill, G.J.P. Britovsek, Polyethylene terephthalate degradation under natural and accelerated weathering conditions, Eur. Polym. J. 136 (2020) 109873. https://doi.org/10.1016/j.eurpolymj.2020.109873.

[21] R. Zhang, X. Ma, X. Shen, Y. Zhai, T. Zhang, C. Ji, J. Hong, PET bottles recycling in China: An LCA coupled with LCC case study of blanket production made of waste PET bottles, J. Environ. Manage. 260 (2020) 110062. https://doi.org/10.1016/j.jenvman.2019.110062.

[22] M.D. de Dios Caputto, R. Navarro, J.L. Valentín, Á. Marcos-Fernández, Chemical upcycling of poly(ethylene terephthalate) waste: Moving to a circular model, J. Polym. Sci. 60 (2022) 3269–3283. https://doi.org/10.1002/pol.20220137.

[23] G.C. Laredo, J. Reza, E. Meneses Ruiz, Hydrothermal liquefaction processes for plastics recycling: A review, Clean. Chem. Eng. 5 (2023) 100094. https://doi.org/10.1016/j.clce.2023.100094.

[24] J. Payne, M.D. Jones, The Chemical Recycling of Polyesters for a Circular Plastics Economy: Challenges and Emerging Opportunities, ChemSusChem. 14 (2021) 4041–4070. https://doi.org/10.1002/cssc.202100400.

[25] M. Khorram, A. Mousavi, N. Mehranbod, Chromium removal using adsorptive membranes composed of electrospun plasma-treated functionalized polyethylene terephthalate (PET) with chitosan, J. Environ. Chem. Eng. 5 (2017) 2366–2377. https://doi.org/10.1016/j.jece.2017.04.010.

[26] S. Roy, P.K. Maji, K.-L. Goh, Sustainable design of flexible 3D aerogel from waste PET bottle for wastewater treatment to energy harvesting device, Chem. Eng. J. 413 (2021) 127409. https://doi.org/10.1016/j.cej.2020.127409.

[27] O. Semyonov, D. Kogolev, G. Mamontov, E. Kolobova, A. Trelin, M.S. Yusubov, O. Guselnikova, P.S. Postnikov, Synergetic effect of UiO-66 and plasmonic AgNPs on PET waste support towards degradation of nerve agent simulant, Chem. Eng. J. 431 (2022) 133450. https://doi.org/10.1016/j.cej.2021.133450.

[28] K. Chan, A. Zinchenko, Conversion of waste bottles' PET to a hydrogel adsorbent via PET aminolysis, J. Environ. Chem. Eng. 9 (2021) 106129. https://doi.org/10.1016/j.jece.2021.106129.

[29] H.N. Doan, P. Phong Vo, K. Hayashi, K. Kinashi, W. Sakai, N. Tsutsumi, Recycled PET as a PDMS-Functionalized electrospun fibrous membrane for oil-

water separation, J. Environ. Chem. Eng. 8 (2020) 103921. https://doi.org/10.1016/j.jece.2020.103921.

[30] Q. Xiong, Q. Tian, X. Yue, J. Xu, X. He, F. Qiu, T. Zhang, Superhydrophobic PET@ZnO Nanofibrous Membrane Extract from Waste Plastic for Efficient Water-In-Oil Emulsion Separation, Ind. Eng. Chem. Res. 61 (2022) 11804–11814. https://doi.org/10.1021/acs.iecr.2c01742.

[31] X. Jin, J. Yuan, J. Shen, Zwitterionic polymer brushes via dopamine-initiated ATRP from PET sheets for improving hemocompatible and antifouling properties, Colloids Surfaces B Biointerfaces. 145 (2016) 275–284. https://doi.org/10.1016/j.colsurfb.2016.05.010.

[32] L.F. Mora-Cortes, A.N. Rivas-Muñoz, M.G. Neira-Velázquez, J.C. Contreras-Esquivel, P. Roger, Y.N. Mora-Cura, G. Soria-Arguello, E.D. Bolaina-Lorenzo, R. Reyna-Martínez, A. Zugasti-Cruz, R.I. Narro-Céspedes, Biocompatible enhancement of poly(ethylene terephthalate) (<scp>PET</scp>) waste films by cold plasma aminolysis, J. Chem. Technol. Biotechnol. 97 (2022) 3001–3010. https://doi.org/10.1002/jctb.7106.

[33] M. Barakzehi, M. Montazer, F. Sharif, T. Norby, A. Chatzitakis, MOF-modified polyester fabric coated with reduced graphene oxide/polypyrrole as electrode for flexible supercapacitors, Electrochim. Acta. 336 (2020) 135743. https://doi.org/10.1016/j.electacta.2020.135743.

[34] Q. Zheng, L. Fang, H. Guo, K. Yang, Z. Cai, M.A.B. Meador, S. Gong, Highly Porous Polymer Aerogel Film-Based Triboelectric Nanogenerators, Adv. Funct. Mater. 28 (2018). https://doi.org/10.1002/adfm.201706365.

[35] M. Shanmugam, C. Chuaicham, A. Augustin, K. Sasaki, P.J.J. Sagayaraj, K. Sekar, Upcycling hazardous metals and PET waste-derived metal–organic frameworks: a review on recent progresses and prospects, New J. Chem. 46 (2022) 15776–15794. https://doi.org/10.1039/D2NJ02481K.

[36] L. Karam, A. Miglio, S. Specchia, N. El Hassan, P. Massiani, J. Reboul, PET waste as organic linker source for the sustainable preparation of MOF-derived methane dry reforming catalysts, Mater. Adv. 2 (2021) 2750–2758. https://doi.org/10.1039/D0MA00984A.

[37] S.-H. Lo, D. Senthil Raja, C.-W. Chen, Y.-H. Kang, J.-J. Chen, C.-H. Lin, Waste polyethylene terephthalate (PET) materials as sustainable precursors for the synthesis of nanoporous MOFs, MIL-47, MIL-53(Cr, Al, Ga) and MIL-101(Cr), Dalt. Trans. 45 (2016) 9565–9573. https://doi.org/10.1039/C6DT01282E.

[38] A.M. Al-Enizi, M. Ubaidullah, J. Ahmed, T. Ahamad, T. Ahmad, S.F. Shaikh, M. Naushad, Synthesis of NiOx@NPC composite for high-performance supercapacitor via waste PET plastic-derived Ni-MOF, Compos. Part B Eng. 183 (2020) 107655. https://doi.org/10.1016/j.compositesb.2019.107655.

[39] E. Cho, S. Yong Lee, J.-W. Choi, S.-H. Kim, K.-W. Jung, Direct upcycling of polyethylene terephthalate (PET) waste bottles into α-Fe2O3 incorporated MIL-53(Al) for the synthesis of Al2O3/Fe3O4-encapsulated magnetic carbon composite and efficient removal of non-steroidal anti-inflammatory drugs, Sep. Purif. Technol. 279 (2021) 119719. https://doi.org/10.1016/j.seppur.2021.119719.

[40] X. Dyosiba, J. Ren, N.M. Musyoka, H.W. Langmi, M. Mathe, M.S. Onyango, Preparation of value-added metal-organic frameworks (MOFs) using waste PET bottles as source of acid linker, Sustain. Mater. Technol. 10 (2016) 10–13. https://doi.org/10.1016/j.susmat.2016.10.001.

[41] M.C. Ribadeneyra, J. King, M.M. Titirici, P.Á. Szilágyi, A facile and sustainable one-pot approach to the aqueous and low-temperature PET-to-UiO-66(Zr) upcycling, Chem. Commun. 58 (2022) 1330–1333. https://doi.org/10.1039/D1CC06250F.

[42] P. He, Z. Hu, Z. Dai, H. Bai, Z. Fan, R. Niu, J. Gong, Q. Zhao, T. Tang, Mechanochemistry Milling of Waste Poly(Ethylene Terephthalate) into Metal–Organic Frameworks, ChemSusChem. 16 (2023). https://doi.org/10.1002/cssc.202201935.

[43] W.P.R. Deleu, I. Stassen, D. Jonckheere, R. Ameloot, D.E. De Vos, Waste PET (bottles) as a resource or substrate for MOF synthesis, J. Mater. Chem. A. 4 (2016) 9519–9525. https://doi.org/10.1039/C6TA02381A.

[44] O. Semyonov, S. Chaemchuen, A. Ivanov, F. Verpoort, Z. Kolska, M. Syrtanov, V. Svorcik, M.S. Yusubov, O. Lyutakov, O. Guselnikova, P.S. Postnikov, Smart recycling of PET to sorbents for insecticides through in situ MOF growth, Appl. Mater. Today. 22 (2021) 100910. https://doi.org/10.1016/j.apmt.2020.100910.

[45] R. Gulyaev, O. Semyonov, G. V. Mamontov, A.A. Ivanov, D.M. Ivanov, M. Kim, V. Švorčík, G. Resnati, T. Liao, Z. Sun, Y. Yamauchi, P.S. Postnikov, O. Guselnikova, Weak Bonds, Strong Effects: Enhancing the Separation Performance of UiO-66 toward Chlorobenzenes via Halogen Bonding, ACS Mater. Lett. 5 (2023) 1340–1349. https://doi.org/10.1021/acsmaterialslett.2c01169.

[46] D. Kogolev, O. Semyonov, N. Metalnikova, M. Fatkullin, R.D. Rodriguez, P.

Slepicka, Y. Yamauchi, O. Guselnikova, R. Boukherroub, P.S. Postnikov, Waste PET upcycling to conductive carbon-based composite through laser-assisted carbonization of UiO-66, J. Mater. Chem. A. 11 (2023) 1108–1115. https://doi.org/10.1039/D2TA08127J.

[47] H. Zhang, X.-L. Zhou, L.-M. Shao, F. Lü, P.-J. He, Upcycling of PET waste into methane-rich gas and hierarchical porous carbon for high-performance supercapacitor by autogenic pressure pyrolysis and activation, Sci. Total Environ. 772 (2021) 145309. https://doi.org/10.1016/j.scitotenv.2021.145309.

[48] G.-T. Xiang, N. Chen, B. Lu, J.-L. Xu, R.D. Rodriguez, E. Sheremet, Y.-D. Hu, J.-J. Chen, Flexible solid-state Zn-Co MOFs@MXene supercapacitors and organic ion hydrogel sensors for self-powered smart sensing applications, Nano Energy. 118 (2023) 108936. https://doi.org/10.1016/j.nanoen.2023.108936.

[49] P. Athanasopoulos, A. Zabaniotou, Post-consumer textile thermochemical recycling to fuels and biocarbon: A critical review, Sci. Total Environ. 834 (2022) 155387. https://doi.org/10.1016/j.scitotenv.2022.155387.

[50] S. Chen, S. Fang, A.I. Lim, J. Bao, Y.H. Hu, 3D meso/macroporous carbon from MgO-templated pyrolysis of waste plastic as an efficient electrode for supercapacitors, Chemosphere. 322 (2023) 138174. https://doi.org/10.1016/j.chemosphere.2023.138174.

[51] X. Liu, Y. Wen, X. Chen, T. Tang, E. Mijowska, Co-etching effect to convert waste polyethylene terephthalate into hierarchical porous carbon toward excellent capacitive energy storage, Sci. Total Environ. 723 (2020) 138055. https://doi.org/10.1016/j.scitotenv.2020.138055.

[52] Z. Fan, J. Ren, H. Bai, P. He, L. Hao, N. Liu, B. Chen, R. Niu, J. Gong, Shape-controlled fabrication of MnO/C hybrid nanoparticle from waste polyester for solar evaporation and thermoelectricity generation, Chem. Eng. J. 451 (2023) 138534. https://doi.org/10.1016/j.cej.2022.138534.

[53] Y. Wen, K. Kierzek, J. Min, X. Chen, J. Gong, R. Niu, X. Wen, J. Azadmanjiri, E. Mijowska, T. Tang, Porous carbon nanosheet with high surface area derived from waste poly(ethylene terephthalate) for supercapacitor applications, J. Appl. Polym. Sci. 137 (2020). https://doi.org/10.1002/app.48338.

[54] M. Ubaidullah, A.M. Al-Enizi, S. Shaikh, M.A. Ghanem, R.S. Mane, Waste PET plastic derived ZnO@NMC nanocomposite via MOF-5 construction for hydrogen and oxygen evolution reactions, J. King Saud Univ. - Sci. 32 (2020) 2397–2405. https://doi.org/10.1016/j.jksus.2020.03.025.

[55] K.-W. Jung, J.-H. Kim, J.-W. Choi, Synthesis of magnetic porous carbon composite derived from metal-organic framework using recovered terephthalic acid from polyethylene terephthalate (PET) waste bottles as organic ligand and its potential as adsorbent for antibiotic tetracycline hydrochlo, Compos. Part B Eng. 187 (2020) 107867. https://doi.org/10.1016/j.compositesb.2020.107867.

[56] T. Ma, W. Wang, R. Wang, Thermal Degradation and Carbonization Mechanism of Fe-Based Metal-Organic Frameworks onto Flame-Retardant Polyethylene Terephthalate, Polymers (Basel). 15 (2023) 224. https://doi.org/10.3390/polym15010224.

[57] Y. Tang, H. Zheng, Y. Wang, W. Zhang, K. Zhou, Laser-Induced Annealing of Metal–Organic Frameworks on Conductive Substrates for Electrochemical Water Splitting, Adv. Funct. Mater. 31 (2021). https://doi.org/10.1002/adfm.202102648.

[58] W. Zhang, R. Li, H. Zheng, J. Bao, Y. Tang, K. Zhou, Laser-Assisted Printing of Electrodes Using Metal–Organic Frameworks for Micro-Supercapacitors, Adv. Funct. Mater. 31 (2021). https://doi.org/10.1002/adfm.202009057.

[59] J. Xu, R. Wang, H. Jiang, X. Liu, L. An, S. Jin, B. Deng, W. Wu, G.J. Cheng, Magnetically Aligned Ultrafine Cobalt Embedded 3D Porous Carbon Metamaterial by One-Step Ultrafast Laser Direct Writing, Adv. Sci. 8 (2021). https://doi.org/10.1002/advs.202102477.

[60] D. Van Lam, V. Nguyen, E. Roh, Q. Ngo, W. Choi, J. Kim, H. Kim, H. Choi, S. Lee, Laser-Induced Graphitic Carbon with Ultrasmall Nickel Nanoparticles for Efficient Overall Water Splitting, Part. Part. Syst. Charact. 38 (2021). https://doi.org/10.1002/ppsc.202100119.

[61] G. Zhao, X. Dong, Y. Du, N. Zhang, G. Bai, D. Wu, H. Ma, Y. Wang, W. Cao, Q. Wei, Enhancing Electrochemiluminescence Efficiency through Introducing Atomically Dispersed Ruthenium in Nickel-Based Metal–Organic Frameworks, Anal. Chem. 94 (2022) 10557–10566. https://doi.org/10.1021/acs.analchem.2c02334.

[62] F. Dubelley, E. Planes, C. Bas, E. Pons, B. Yrieix, L. Flandin, The hygrothermal degradation of PET in laminated multilayer, Eur. Polym. J. 87 (2017) 1–13. https://doi.org/10.1016/j.eurpolymj.2016.12.004.

[63] I.M. Ward, M.A. Wilding, Infra-red and Raman spectra of poly(m-methylene terephthalate) polymers, Polymer (Guildf). 18 (1977) 327–335. https://doi.org/10.1016/0032-3861(77)90077-5.

[64] H. Chang, Y. Zhou, S. Zhang, X. Zheng, Q. Xu, CO 2 -Induced 2D Ni-BDC Metal–

Organic Frameworks with Enhanced Photocatalytic CO 2 Reduction Activity, Adv. Mater. Interfaces. 8 (2021). https://doi.org/10.1002/admi.202100205.

[65] L.L. Mguni, Y. Yao, J. Ren, X. Liu, D. Hildebrandt, Modulated synthesized Ni-based MOF with improved adsorptive desulfurization activity, J. Clean. Prod. 323 (2021) 129196. https://doi.org/10.1016/j.jclepro.2021.129196.

[66] L. Ai, N. Li, M. Chen, H. Jiang, J. Jiang, Photothermally boosted water splitting electrocatalysis by broadband solar harvesting nickel phosphide within a quasi-MOF, J. Mater. Chem. A. 9 (2021) 16479–16488. https://doi.org/10.1039/D1TA02995A.

[67] L. Xia, Q. Zhang, X. Zhuang, S. Zhang, C. Duan, X. Wang, B. Cheng, Hot-Pressed Wet-Laid Polyethylene Terephthalate Nonwoven as Support for Separation Membranes, Polymers (Basel). 11 (2019) 1547. https://doi.org/10.3390/polym11101547.

[68] D. Zhu, J. Liu, L. Wang, Y. Du, Y. Zheng, K. Davey, S.-Z. Qiao, A 2D metal–organic framework/Ni(OH) 2 heterostructure for an enhanced oxygen evolution reaction, Nanoscale. 11 (2019) 3599–3605. https://doi.org/10.1039/C8NR09680E.

[69] A. Lipovka, I. Petrov, M. Fatkullin, G. Murastov, A. Ivanov, N.E. Villa, S. Shchadenko, A. Averkiev, A. Chernova, F. Gubarev, M. Saqib, W. Sheng, J.-J. Chen, O. Kanoun, I. Amin, R.D. Rodriguez, E. Sheremet, Photoinduced flexible graphene/polymer nanocomposites: Design, formation mechanism, and properties engineering, Carbon N. Y. 194 (2022) 154–161. https://doi.org/10.1016/j.carbon.2022.03.039.

[70] D.A. Sokolov, C.M. Rouleau, D.B. Geohegan, T.M. Orlando, Excimer laser reduction and patterning of graphite oxide, Carbon N. Y. 53 (2013) 81–89. https://doi.org/10.1016/j.carbon.2012.10.034.

[71] V. Strong, S. Dubin, M.F. El-Kady, A. Lech, Y. Wang, B.H. Weiller, R.B. Kaner, Patterning and Electronic Tuning of Laser Scribed Graphene for Flexible All-Carbon Devices, ACS Nano. 6 (2012) 1395–1403. https://doi.org/10.1021/nn204200w.

[72] E. Kymakis, K. Savva, M.M. Stylianakis, C. Fotakis, E. Stratakis, Flexible Organic Photovoltaic Cells with In Situ Nonthermal Photoreduction of Spin-Coated Graphene Oxide Electrodes, Adv. Funct. Mater. 23 (2013) 2742–2749. https://doi.org/10.1002/adfm.201202713.

[73] J. Ren, C. Wang, X. Zhang, T. Carey, K. Chen, Y. Yin, F. Torrisi, Environmentally-friendly conductive cotton fabric as flexible strain sensor based on hot press

reduced graphene oxide, Carbon N. Y. 111 (2017) 622–630. https://doi.org/10.1016/j.carbon.2016.10.045.

[74] T. Raza, M.K. Tufail, A. Ali, A. Boakye, X. Qi, Y. Ma, A. Ali, L. Qu, M. Tian, Wearable and Flexible Multifunctional Sensor Based on Laser-Induced Graphene for the Sports Monitoring System, ACS Appl. Mater. Interfaces. 14 (2022) 54170–54181. https://doi.org/10.1021/acsami.2c14847.

[75] L. Cheng, G. Fang, L. Wei, W. Gao, X. Wang, Z. Lv, W. Xu, C. Ding, H. Wu, W. Zhang, A. Liu, Laser-Induced Graphene Strain Sensor for Conformable Lip-Reading Recognition and Human–Machine Interaction, ACS Appl. Nano Mater. 6 (2023) 7290–7298. https://doi.org/10.1021/acsanm.3c00410.

[76] S. Hong, J. Kim, S. Jung, J. Lee, B.S. Shin, Surface Morphological Growth Characteristics of Laser-Induced Graphene with UV Pulsed Laser and Sensor Applications, ACS Mater. Lett. 5 (2023) 1261–1270. https://doi.org/10.1021/acsmaterialslett.2c01222.

[77] H. Liu, K. Chen, R. Wu, S. Pan, C. Zhang, Laser-Induced Graphene-based Flexible Substrate with Photothermal Conversion and Photoresponse Performance on Polyimide Film, ACS Appl. Mater. Interfaces. 15 (2023) 46550–46558. https://doi.org/10.1021/acsami.3c10729.

[78] Y.C. Guan, Y.W. Fang, G.C. Lim, H.Y. Zheng, M.H. Hong, Fabrication of Laser-reduced Graphene Oxide in Liquid Nitrogen Environment, Sci. Rep. 6 (2016) 28913. https://doi.org/10.1038/srep28913.

[79] I.I. Bobrinetskiy, A.V. Emelianov, S.A. Smagulova, I.A. Komarov, N. Otero, P.M. Romero, Laser direct 3D patterning and reduction of graphene oxide film on polymer substrate, Mater. Lett. 187 (2017) 20–23. https://doi.org/10.1016/j.matlet.2016.10.073.

[80] R. Rahimi, M. Ochoa, W. Yu, B. Ziaie, Highly Stretchable and Sensitive Unidirectional Strain Sensor via Laser Carbonization, ACS Appl. Mater. Interfaces. 7 (2015) 4463–4470. https://doi.org/10.1021/am509087u.

[81] A.R. Cardoso, A.C. Marques, L. Santos, A.F. Carvalho, F.M. Costa, R. Martins, M.G.F. Sales, E. Fortunato, Molecularly-imprinted chloramphenicol sensor with laser-induced graphene electrodes, Biosens. Bioelectron. 124–125 (2019) 167–175. https://doi.org/10.1016/j.bios.2018.10.015.

[82] L. Cao, S. Zhu, B. Pan, X. Dai, W. Zhao, Y. Liu, W. Xie, Y. Kuang, X. Liu, Stable and durable laser-induced graphene patterns embedded in polymer substrates, Carbon N. Y. 163 (2020) 85–94. https://doi.org/10.1016/j.carbon.2020.03.015.

[83] J. Edberg, R. Brooke, O. Hosseinaei, A. Fall, K. Wijeratne, M. Sandberg, Laser-induced graphitization of a forest-based ink for use in flexible and printed electronics, Npj Flex. Electron. 4 (2020) 17. https://doi.org/10.1038/s41528-020-0080-2.

[84] R.D. Rodriguez, S. Shchadenko, G. Murastov, A. Lipovka, M. Fatkullin, I. Petrov, T. Tran, A. Khalelov, M. Saqib, N.E. Villa, V. Bogoslovskiy, Y. Wang, C. Hu, A. Zinovyev, W. Sheng, J. Chen, I. Amin, E. Sheremet, Ultra-Robust Flexible Electronics by Laser-Driven Polymer-Nanomaterials Integration, Adv. Funct. Mater. 31 (2021). https://doi.org/10.1002/adfm.202008818.

[85] M.-S. Wu, W.-H. Hsu, Nickel nanoparticles embedded in partially graphitic porous carbon fabricated by direct carbonization of nickel-organic framework for high-performance supercapacitors, J. Power Sources. 274 (2015) 1055–1062. https://doi.org/10.1016/j.jpowsour.2014.10.133.

[86] A. Furlan, J. Lu, L. Hultman, U. Jansson, M. Magnuson, Crystallization characteristics and chemical bonding properties of nickel carbide thin film nanocomposites, J. Phys. Condens. Matter. 26 (2014) 415501. https://doi.org/10.1088/0953-8984/26/41/415501.

[87] Y. Wu, Z. Huang, H. Jiang, C. Wang, Y. Zhou, W. Shen, H. Xu, H. Deng, Facile Synthesis of Uniform Metal Carbide Nanoparticles from Metal–Organic Frameworks by Laser Metallurgy, ACS Appl. Mater. Interfaces. 11 (2019) 44573–44581. https://doi.org/10.1021/acsami.9b13864.

[88] R.D. Rodriguez, S. Shchadenko, G. Murastov, A. Lipovka, M. Fatkullin, I. Petrov, T. Tran, A. Khalelov, M. Saqib, N.E. Villa, V. Bogoslovskiy, Y. Wang, C. Hu, A. Zinovyev, W. Sheng, J. Chen, I. Amin, E. Sheremet, Ultra-Robust Flexible Electronics by Laser-Driven Polymer-Nanomaterials Integration, Adv. Funct. Mater. 31 (2021) 2008818. https://doi.org/10.1002/adfm.202008818.

[89] M.-C. Liu, Y.-M. Hu, W.-Y. An, Y.-X. Hu, L.-Y. Niu, L.-B. Kong, L. Kang, Construction of high electrical conductive nickel phosphide alloys with controllable crystalline phase for advanced energy storage, Electrochim. Acta. 232 (2017) 387–395. https://doi.org/10.1016/j.electacta.2017.02.169.

[90] A.I.A. Soliman, A.-M.A. Abdel-Wahab, H.N. Abdelhamid, Hierarchical porous zeolitic imidazolate frameworks (ZIF-8) and ZnO@N-doped carbon for selective adsorption and photocatalytic degradation of organic pollutants, RSC Adv. 12 (2022) 7075–7084. https://doi.org/10.1039/D2RA00503D.

[91] Y. Hu, H. Yao, Q. Liao, T. Lin, H. Cheng, L. Qu, The promising solar-powered

water purification based on graphene functional architectures, EcoMat. 4 (2022). https://doi.org/10.1002/eom2.12205.

[92] A.K. Pathak, M. Borah, A. Gupta, T. Yokozeki, S.R. Dhakate, Improved mechanical properties of carbon fiber/graphene oxide-epoxy hybrid composites, Compos. Sci. Technol. 135 (2016) 28–38. https://doi.org/10.1016/j.compscitech.2016.09.007.

[93] Y. Han, Y. Han, X. Zhang, L. Li, C. Zhang, J. Liu, G. Lu, H.-D. Yu, W. Huang, Fish Gelatin Based Triboelectric Nanogenerator for Harvesting Biomechanical Energy and Self-Powered Sensing of Human Physiological Signals, ACS Appl. Mater. Interfaces. 12 (2020) 16442–16450. https://doi.org/10.1021/acsami.0c01061.

[94] A. Lipovka, M. Fatkullin, S. Shchadenko, I. Petrov, A. Chernova, E. Plotnikov, V. Menzelintsev, S. Li, L. Qiu, C. Cheng, R.D. Rodriguez, E. Sheremet, Textile Electronics with Laser-Induced Graphene/Polymer Hybrid Fibers, ACS Appl. Mater. Interfaces. 15 (2023) 38946–38955. https://doi.org/10.1021/acsami.3c06968.

[95] H. Yang, S. Ji, I. Chaturvedi, H. Xia, T. Wang, G. Chen, L. Pan, C. Wan, D. Qi, Y.-S. Ong, X. Chen, Adhesive Biocomposite Electrodes on Sweaty Skin for Long-Term Continuous Electrophysiological Monitoring, ACS Mater. Lett. 2 (2020) 478–484. https://doi.org/10.1021/acsmaterialslett.0c00085.

[96] Z. Lou, S. Chen, L. Wang, R. Shi, L. Li, K. Jiang, D. Chen, G. Shen, Ultrasensitive and ultraflexible e-skins with dual functionalities for wearable electronics, Nano Energy. 38 (2017) 28–35. https://doi.org/10.1016/j.nanoen.2017.05.024.

[97] J. Cao, C. Lu, J. Zhuang, M. Liu, X. Zhang, Y. Yu, Q. Tao, Multiple Hydrogen Bonding Enables the Self-Healing of Sensors for Human–Machine Interactions, Angew. Chemie. 129 (2017) 8921–8926. https://doi.org/10.1002/ange.201704217.